The influence of cold rolling and hydroxyapatite coating on the mechanostructure, corrosion resistance, cell viability, and antibacterial activity of ZnCu biodegradable implants

B. Aksakal[1,a)], S. A. Karadogan[2], N. Aslan[3,4], F. Fidan[5], Y. Yilmazer[6], S. Sezek[7]

[1] Department of Aircraft Fuselage Engine, School of Civil Aviation, Firat University, Elazig, Turkey
[2] Graduate School of Science and Engineering, Yildiz Technical University, Istanbul, Turkey
[3] Department of Metallurgical and Materials Engineering, Munzur University, Tunceli, Turkey
[4] Rare Earth Elements Application and Research Center, Munzur University, Tunceli, Turkey
[5] 100/2000 YÖK (Council of Higher Education) Doctoral Grant Recipient, Institute of Post Graduate Education, Munzur University, Tunceli, Turkey
[6] Department of Molecular Biology and Genetics, Sabahattin Zaim University, Istanbul, Turkey
[7] Department of Mechanical Engineering, Atatürk University, Erzurum, Turkey
a) Address all correspondence to this author. e-mail: baksakal@firat.edu.tr

Zinc (Zn) and its alloys exhibit great potential for utilization in biodegradable bone implants. Zn-1Cu biodegradable alloy was produced and were cold rolled at two different deformation rates of 47 and 61%. The samples have been bioceramic coated with the sol–gel method and microstructure-mechanical property changes, corrosion behavior and biocompatibility of the samples were investigated. They were characterized by Optical, SEM, XRD and wettability analysis. The rolled samples showed a significant increase in hardness when compared to the non-rolled samples. The unrolled and 47% rolled samples showed better corrosion resistance compared to 61% rolled samples. Antibacterial effects of the base and sol–gel-coated groups showed higher cell viability ratios than the uncoated groups. Cell viability increased significantly in 47% of the rolled samples after 24, 48, and 72 h, however decreased by up to 70% in 61% of the rolled samples.

Introduction

Biomedical materials are implanted in the body to treat, replace, or regenerate non-functional tissues. Such materials must be extremely load-resistant, non-toxic, and capable of performing the same functions as the limb or tissue being replaced [1, 2]. These materials' internal structure, mechanical properties, and surface features make them more appealing alternatives for implant and stent materials than their polymeric counterparts [3]. Zinc-based metallic alloys have received a great deal attention in recent years as a biodegradable material [4, 5]. The research of "bioabsorbable" functioning stents to prevent long-term negative effects while making stents more biocompatible and corrosion resistant is still ongoing [6]. In some biomedical applications, the substance is predicted to be biodegradable and deteriorate slowly, extending the tissue's life and eliminating the need for reoperation. However, they have some drawbacks, including inadequate biocompatibility and bioactivity, as well as corrosion and abrasion-prone behavior [7, 8].

The efficacy of biodegradable materials as temporary filling materials for tissue connection, strengthening, and support has been reported. These materials offer a potential solution to the drawbacks associated with insoluble materials, including persistent irritation, mechanical incompatibilities, limited adaptability to growth in young patients, and long-term chronic inflammation. [9]. They offer numerous benefits compared to conventional biomaterials. Such as the elimination of the necessity for a subsequent surgical procedure, which can have adverse effects on the patient's comfort and psychological well-being, as well as potentially causing tissue damage. Consequently, the risk of infection is diminished. Additionally, there are no issues such as tissue release or deformation. These materials are utilized for several purposes, including stent placement, management of

coronary artery or circulatory system obstructions, correction of bone deformities, and treatment of limbs such as the arms and legs [10].

Zinc, being the primary constituent of biodegradable materials, plays a crucial role as a nutritional factor in the growth and development of both humans and animals. Zinc deficiency has been linked to impaired bone development, while it has been documented to possess a restorative impact on bone loss in diverse pathophysiological circumstances, such as deficiencies in calcium and vitamin D, estrogen, diabetes, and fracture healing [11]. Zinc-based materials have promising characteristics as prospective candidates for biodegradable metallic stents due to their possession of the necessary mechanical and biodegradation qualities essential for achieving optimal stent performance [11].

Nevertheless, in recent years, there has been a rise in the development of innovative methods to enhance Zn-based biomaterials in stents and other applications. This is mostly due to their low corrosion rate and mechanical capabilities, which can be enhanced by using various alloys without generating harmful byproducts after corrosion [12, 13]. The wear resistance of Zn–Al–Cu alloys was assessed in a study, whereby different quantities of copper were incorporated [14]. Alternatively, researchers have investigated the possibility of Zn–Mg alloys with a maximum Mg content of 3 wt% as biodegradable materials for medical applications [15]. Another study investigated the use of Zn alloys for vascular stent applications and found that Fe significantly influenced the microstructure, mechanical characteristics, and corrosion resistance of the alloy [16, 17]. The study found that subjecting Cu-based biodegradable materials to cold treatments led to the formation of evenly distributed CuZn4 precipitates within the structure [18].

Recent studies have explored alternate biodegradable materials, such as Zn-based compounds, in addition to Fe and Mg alloying, and these materials have shown potential for orthopedic implants [19, 20]. Nevertheless, despite the advantages of these materials, such as their moderate corrosion rate, moderate biocompatibility, lack of toxic corrosion byproducts, ease of processing, low melting point, and reduced reactivity in the molten state, they also possess limitations, including low mechanical strength and age hardening. Consequently, extensive research has been conducted to enhance and safeguard these materials [21]. Metallic implants have been coated with hydroxyapatite and bioceramic-based materials utilizing a variety of ways to improve their bioactive performance and protect them [3, 21]. There is no comprehensive investigation of Zn-based biodegradable materials, and most studies focus on manufacturing, mechanical characteristics, or corrosion resistance [21–23]. The present study focused on the synthesis of Zn-1Cu biodegradable alloys by the utilization of the arc melting and casting technique. The samples were subjected to cold rolling and a sol–gel coating of HA-based bioceramic in order to improve their performance

as a biodegradable material for implants. The impact of various treatments on the morphological, mechanical, corrosion, antibacterial, and cell viability properties of Zn-1Cu was evaluated.

Results and discussion

In this section, microstructure, mechanical tests, coating processes, corrosion tests, antimicrobial and cell viability results of treated biodegradable Zn1Cu samples are presented. For Zn-1Cu alloy; 3 different groups were studied as unrolled, 47% rolled and 61% rolled and the morphological, mechanical, corrosive and biocompatibility effects of rolling process and bioceramic coating on Zn alloy were shown.

Micro-structure characterizations

Before optical analysis, the rolled and unrolled samples were subjected to annealing at 200 °C for 1 h and the changes in optical views were shown in Fig. 1(a–e). Figure 1(a, b) shows the microstructure images of Zn-1Cu samples with and without rolling before and after heat treatment. In the images obtained, grain boundaries and single phase were observed and no secondary phase was observed. The grain structure consisted of relatively large and inhomogeneous grain structures, and voids and crack defects from casting were observed in the structure.

Rolling and annealing caused the same flaws to be larger and orientated in 47% of the rolled specimens [Fig. 1(c, d)]. While some grain boundaries are obvious, others are oriented along the rolling direction, and grain sizes become thinner and longer as the rolling progresses. The SEM images also show the formation of Cu-containing precipitates at the grain boundaries [Fig. 1(c, e)]. In the 61% rolled sample, these flaws and orientations became much more evident, and a secondary phase structure developed. It was found that the grains and grain boundaries, which were extended and twisted after rolling due to recrystallization in the rolled samples, were more effective and uniformly dispersed after annealing. The 61% rolled sample had much higher small grain visibility, and the porosity structure and fissures induced by casting and rolling were significantly decreased. The CuZn5 phase formed as a secondary phase after rolling, and when the optical images in Fig. 1(e–f) were examined, it was observed that Zn–Cu phase structures spread over the sample surface after rolling, and Zn grains became thinner by clustering around the created CuZn5 phase. [24, 25].

SEM images of rolled-uncoated and sol–gel HA based coatings are given in Fig. 2(a–c). In the pre-coating images, the main matrix Zn and Cu grains were observed and Cu-rich precipitates were formed at the grain boundaries [26]. In the unrolled and uncoated SEM image, surface deformations are more pronounced and microcracks and hollow porous structures are located on the surface. The unrolled sample has a relatively more
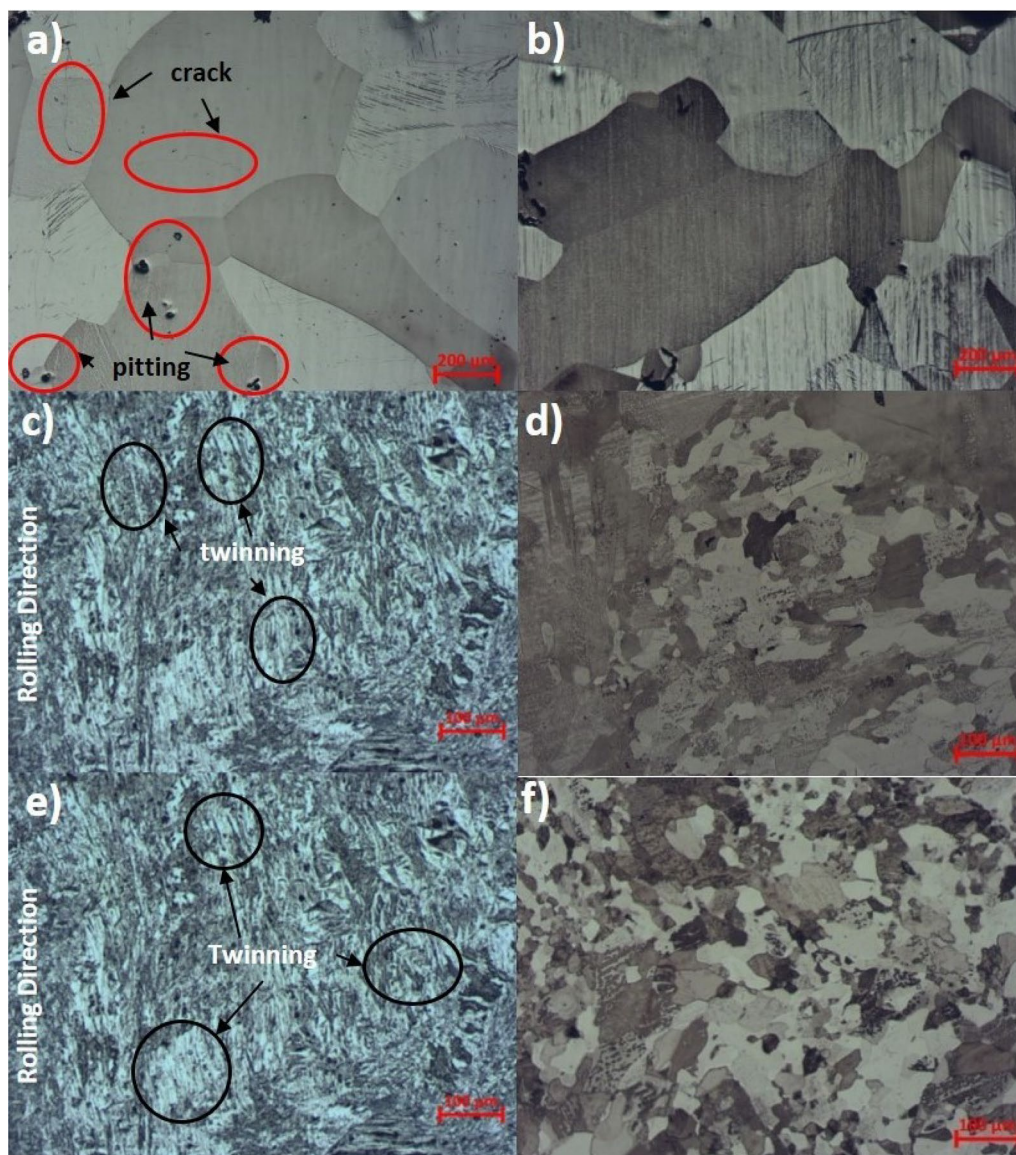
Figure 1: Optical images of (a) unannealed and (b) 1 h annealed at 200 °C after casting, (c) 47% post-rolling-no annealing (d) 47% post-rolling 1 h annealed at 200 °C, (e) 61% post-rolling-no annealing, (f) 61% post-rolling-1 h annealed at 200 °C.

homogeneous structure than the rolled samples, while the grain orientations are observed to be random rather than in a single direction [Fig. 2(a)]. The pre-coating EDS spectra, as well as the Ca and P peaks of the samples prior to and following HA coating, are clearly apparent. The presence of Si in this spectrum can be attributed to the abrasive employed to prepare the sample surfaces.

Figure 2(b and c) show comparative SEM pictures and EDS analysis results before and after coating for 47 and 61% cold rolled Zn1Cu samples. The grain orientations after rolling exhibit a complicated structure towards the rolling direction. As the cold rolling pass rate rose from 47% [Fig. 2(b)] to 61% [Fig. 2(c)], more flaws were identified, and the microcracks in the non-rolled samples became more visible with rolling. Because of the high deformation, significant voids and irregular structures formed in the structure of the 61% rolled sample [Fig. 2(c)], and cracks induced by casting defects expanded in the direction of deformation, making it difficult to identify grain boundaries at both rolling rates. The primary difference in surface morphology after coating is that the dominant Zn image of the Zn-1Cu substrate structure in the uncoated sample has transformed into a layer created by the presence of several elements (Ca, P, O, Cl). Although the porous nature of the casting was partially filled after coating, holes, pits, and porosities were still visible in some areas. The coated surface had oval-shaped and small HA-based grains, and it was less abraded and
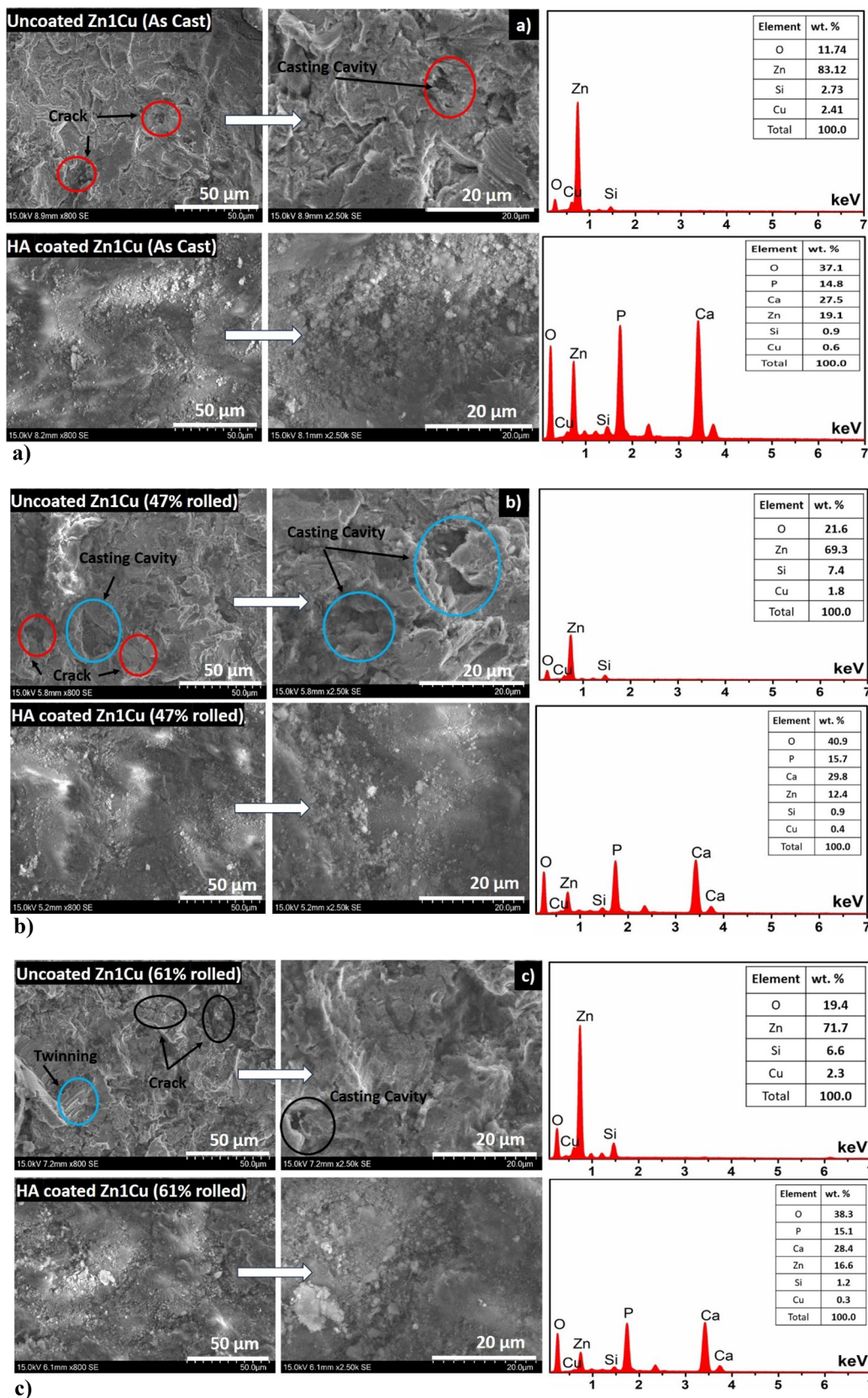
Figure 2: SEM–EDS analysis of Zn1Cu alloy, (a) uncoated and HA-coated, (b) uncoated, 47% cold rolled and HA-coated, (c) uncoated, 61% cold rolled and HA-coated.

smoother than the uncoated sample. The surface morphology of the unrolled and rolled specimens after coating showed great similarities. In the rolled specimens, grain boundaries and orientations disappeared, pits and voids formed after rolling were reduced, microcracks on the surface were filled by the coating and became invisible. It was observed that the coating covered the sample surface and consisted of HA structures from the coating; according to EDS analysis, these new structures (Ca, P, O) were determined to be the main components of HA.

XRD spectra of uncoated and HA coated cast, 47% and 61% Zn1Cu alloys are shown in Fig. 3(a and b), respectively. It shows that the unrolled sample before coating consists of Zn only, while the rolled (47% and 61%) Zn-1Cu structures consist of Zn and CuZn5 phase. All samples showed Zn peaks at $2\theta = 36.52, 38.76, 43.16, 54.42, 70.40, 77.82, 82.10$ and 86.34, and high Zn peak intensities were observed in the unrolled sample at $2\theta = 36.52$ and 77.82. Among the rolled samples, CuZn5 phase is observed at low intensities and peaks at $2\theta = 37.42, 41.94, 57.50, 67.62$ and 83.54. In the unrolled Zn-1Cu spectrum, no peak belonging to the CuZn5 phase was observed, while the CuZn5 phase seen with rolling is thought to be the main reason for the increase in hardness.

Zn was detected in the XRD study after coating, as well as at areas where Zn peaked before to coating. In uncoated samples, no peak was found before $2\theta = 35$. However, HA structures were observed at $2\theta = 25.66°, 28.70°, 31.68°, 32.74°, 33.90°, 46.78°$, and $49.46°$ following HA coating. No significant differences were found between the unrolled and rolled samples, and it is worth noting that the visibility of the rolling effect decreased in the XRD examination after coating. All samples had Zn peaks at $2\theta = 36.38°, 38.64°, 42.98°, 57.30°, 70.28°, 81.96°, 83.48°$ and 86.22° points. Rolled samples had higher peak intensity at $2\theta = 42.98°, 81.96°$ and $83.48°$ points.

Mechanical tests: hardness and compression

Hardness and compression tests were carried out for uncoated-unrolled and rolled (47% and 61%) specimens [Fig. 4(b)]. Four measurements were taken for the microhardness values of the samples for unrolled, 47% rolled, and 61% rolled and the average of these values was then used to determine the hardness values for each sample [Fig. 4(a)].

The average hardness values obtained were 57.9 HV for unrolled specimens, 74.9 HV for 47% rolled specimens and 72.3 HV for 61% rolled specimens. The hardness value of 57.9 HV for the cast specimen (unrolled) was close to the 63 ± 2 HV hardness value as reported in the literature [27]. As anticipated, the hardness values of the Zn alloy improved significantly when subjected to rolling, with a 29.36% rise observed for 47% rolling and a 24.87% increase for 61% rolling. This result may be related to the breakage of the CuZn5 phase and its dispersion along the grain orientation and grain refinement [28]. The sample with a roll percentage of 47% exhibited the highest hardness, but the sample with a roll percentage of 61% displayed a lesser hardness, albeit with a similar value. This can be interpreted that the CuZn5 solid precipitate in the rolled alloy of the highly rolled alloy may have been broken and reduced the hardness [29]. Furthermore, it can be stated that the empty spaces created during the casting process merge together as the rolling process intensifies, resulting in the development of small cracks, the formation of recrystallized grains, and a reduction in Cu orientation and hardness in the 61% rolled sample [30].
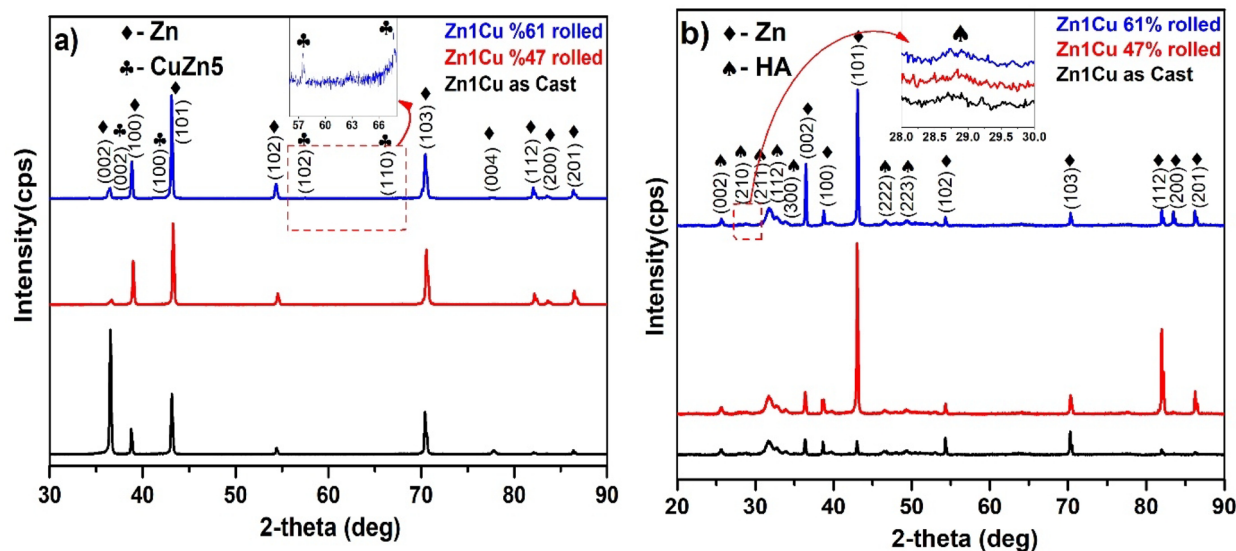

Figure 3: XRD spectra of uncoated (a) and HA-coated (b) unrolled, 47% rolled and 61% rolled Zn1Cu samples.
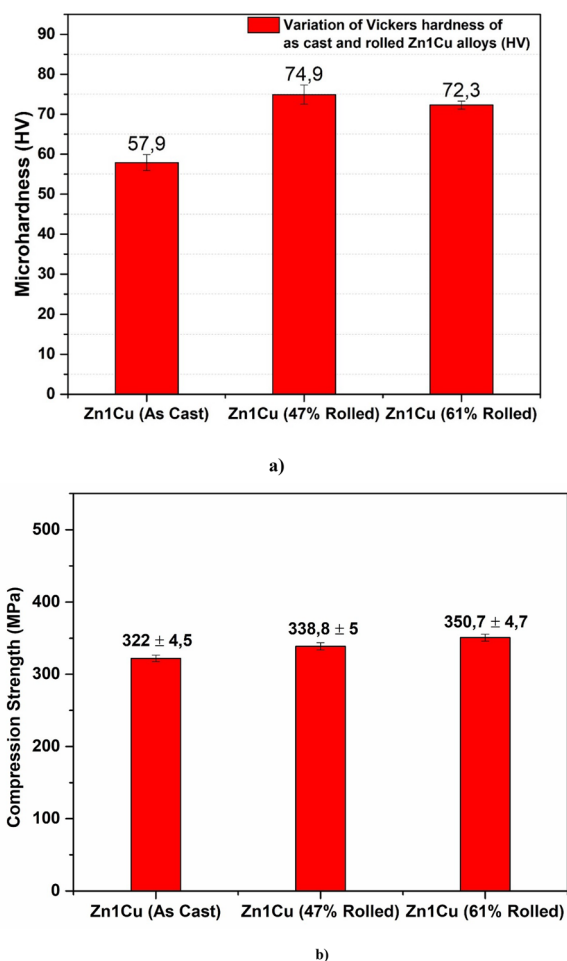
Figure 4: Mechanical test results (a) Microhardness values of cast, 47% and 61% rolled and (b) Compression Strength of cast, 47% and 61% rolled Zn1Cu alloy.

Compression tests were conducted on both cast (unrolled) and rolled specimens, with 47% and 61% of the specimens being subjected to these tests and the test results are presented in Fig. 4(b). Compression tests were conducted using three specimens from each group, consisting of three specimens from the cast group and two specimens from the rolling group. According to these results; 322 ± 4.5 MPa for unrolled specimen, 338.8 ± 5 MPa for 47% rolled specimen and 350.7 ± 4.7 MPa for 61% rolled specimen. It has been shown in various studies that Zn–Cu alloy provides better mechanical properties than pure Zn [24, 27]. It was observed that the mechanical properties increased as expected with the increase in rolling ratio. The observed phenomenon is believed to be attributed to the increased visibility of the Ɛ-CuZn5 solid precipitate phase during the rolling process, resulting in a reduction in grain thickness and an elongation of the grains in the direction of rolling. Upon examination of the optical and scanning electron microscopy (SEM) images of the

biodegradable Zn-1Cu alloy rolled at various ratios, it was seen that the precipitate of micron-sized size was dispersed both along the grain boundaries and within the grain (Figs. 1–2). A large number of CuZn5 phases with micron and submicron sizes are formed from supersaturated solid solution during cold rolling [31]. In addition, although high deformation rates caused distortions in the main matrix Zn phase, the CuZn5 phase was denser on the surface after rolling. Accordingly, the higher appearance of CuZn5 phase in the grain after rolling caused an increase in the compressive strength of the samples.

Wettability analysis

Wettability analysis and contact angle measurement results are of great importance for coating and cell adhesion performance. The smaller the contact angle and the higher the surface energy, the stronger the hydrophilicity of the materials and this provides a more conductive surface that provides better cell adhesion [32, 33].

Contact angle measurements with uncoated samples gave 98.530, 108.160, and 107.970 angles for the unrolled sample, 47% rolled sample, and 61% rolled sample, respectively, with no discernible difference between the rolled samples. Another study reported a contact angle of $62.4° \pm 0.9°$ for cast Zn-1Cu [34], while pure Zn as an orthopaedic implant had a contact angle of 82.8 ± 2.40 [35]. Figure 5 shows the wettability analysis findings for both unrolled and rolled specimens. According to these findings, all specimens exhibited hydrophobic qualities, with the best specimen being 47% rolled [Fig. 5(b)], followed by 61% rolled [Fig. 5(c)], and unrolled [Fig. 5(a)].

The poor wettability performance of Zn alloys is due to the susceptibility of Zn to oxidation and the large surface tensions resulting from the large amount of Zn elements [36]. Unrolled Zn showed the lowest hydrophobic properties, while the hydrophilic properties were better than the rolled samples. The optic microscopy study (Fig. 1) showed that the voids and cracks in the unrolled sample do not extend throughout the surface and have a low density distribution, resulting in enhanced wettability performance [37]. It has previously been shown that hydrophilicity is an important feature for cardiovascular stents because it promotes cell attachment on the material surface [32].

Specimens with hydrophilic characteristics can help produce better coatings due to the adhesive force effect (liquid attraction) of the specimen surface. It is believed that all of the samples are hydrophobic due to Zn's low wettability performance and the fact that rolling spreads the fractures in the sample. For these reasons, it was concluded that the sample with the closest results to the intended values was the one that succeeded without rolling. It was also found that after coating the sample, the coating's wettability qualities varied depending on the methods of application [38].
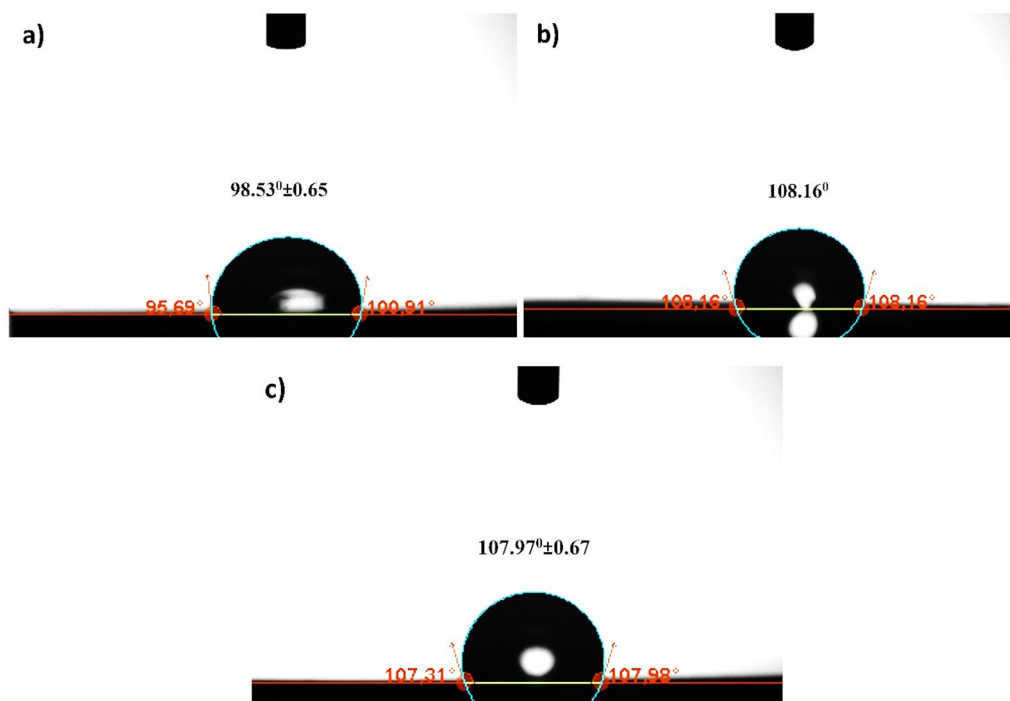
Figure 5: Wettability analyses of the samples (a) without rolled, (b) with 47% rolled and (c) with 61% rolled.

Corrosion tests

Because of the aggressive ions such as chlorine in the solution content, medium and low corrosion resistant metals (such as Zn, Cu, Ni) tend to be oxidized in the OCP stage without passing through the dynamic potential screening (PDS) stage, as shown in Reactions 1 and 2.

$$Zn \rightarrow Zn^{2+} + 2e^{-}, \qquad (1)$$

$$Cu \rightarrow Cu^{2+} + 2e^{-}, \qquad (2)$$
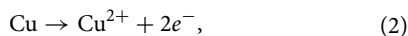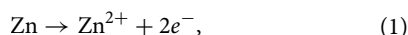
In this study, PDS curves obtained before and after sol–gel bioceramic coating are given in Fig. 6(a, b) and corrosion parameters calculated from PDS curves are given in Table 1. When the PDS curves for each sample are analyzed, Zn1Cu/HA and Zn1Cu samples are analyzed at − 1.02 and − 1 V potential values, Zn1Cu (47%) and Zn1Cu (61%) samples are analyzed at − 1.02 and − 0.96 V potential values, ZnCu/HA (47%rd) and ZnCu/HA (61%rd) samples are analyzed at − 1. 02 and − 0.93 V potential values, respectively, relatively parallel to the potential
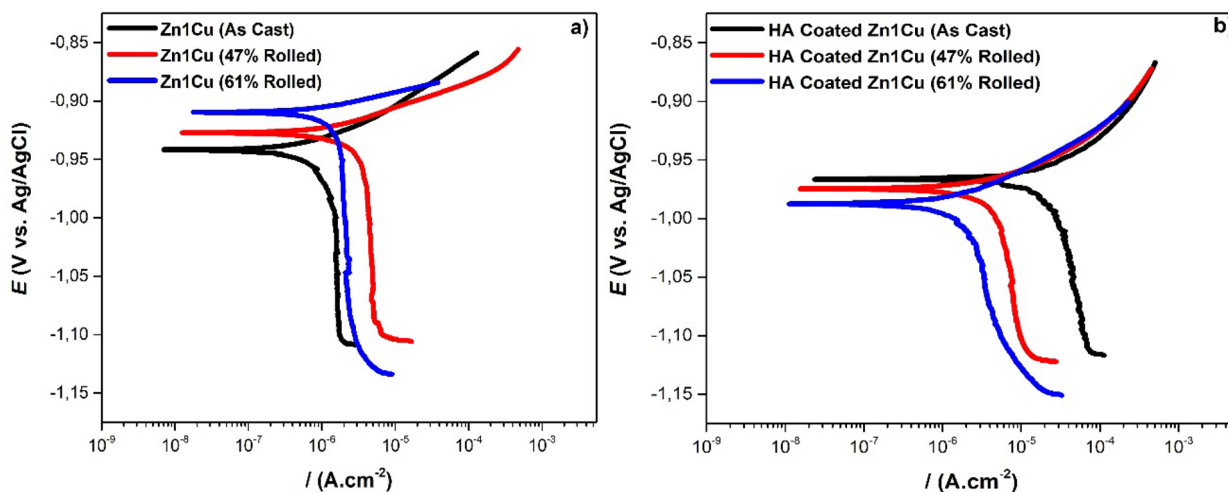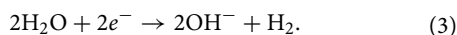

Figure 6: Potentiodynamic scanning (PDS) curves of uncoated (a), hydroxyapatite (HA)-coated (b) cast, 47% and 61% cold rolled Zn-1Cu alloy.

axis, and this behavior is generally directly related to the hydrogen gas production in Reaction 3 [39].

$$2H_2O + 2e^- \rightarrow 2OH^- + H_2. \qquad (3)$$

Then, in the cathodic region, which oscillates with a slope to the corrosion potential as observed in the PDS curves of all samples, oxygen consumption reactions continue with Reactions 4 and 5.

$$O_2 + H_2O + 2e^- \rightarrow HO_2^- + OH^-, \qquad (4)$$

$$O_2 + H_2O + 2e^- \rightarrow HO_2^- + OH^-. \qquad (5)$$
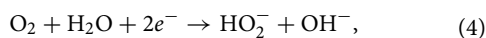
It was observed that the uncoated samples shifted towards higher E_{corr} value as the rolling ratio increased and after coating, it was observed that it shifted towards lower E_{corr} value as the rolling ratio increased.

When conducting a quantitative analysis of the values reported in Table 1, it was noticed that there was a negligible increase (5% and 10%) in the thermodynamic data, Ecorr values of the HA coated samples. Additionally, the kinetic data J_{corr} was evaluated to compare corrosion [40]. It was observed that the J_{corr} value of the HA coated Zn-1Cu precursor was about 40% higher than the uncoated sample, and the coated and uncoated 61% rolled Zn-1Cu samples gave similar J_{corr} values. Nevertheless, it was revealed that the sole specimen exhibiting enhanced resistance to corrosion was the HA-coated 47% rolled Zn-1Cu sample, which demonstrated a reduction of around 44% in the J_{corr} value. Upon comparing the βc values, it becomes evident that the observed increase in corrosion resistance can be attributed to the deceleration of cathodic processes. It is highly probable that the lack of the expected increase in corrosion resistance with coating is due to the porous coating that does not uniformly cover the entire surface [Fig. 1(d and f)] [41] and the porous HA coating may have caused an increase in the localized corrosion rate because the current is concentrated in the uncoated but conductive regions between the relatively nonconductive HA coated surface [41]. A similar interpretation can be made between unrolled and rolled specimens. The higher E_{corr} and lower J_{corr} susceptibility of the unrolled specimens compared to the rolled specimens may be due to the increased visibility of post-rolling pores and porosities on the specimen surface of the rolled specimens [Fig. 1(c and e)].

SEM images of uncoated and coated specimens after corrosion tests are given in Fig. 7. It is noteworthy that the surface nonhomogeneities of the pre-coating specimens deepened and widened after corrosion. The unrolled specimens show large and deep cracks, while the rolled specimens show deep voids as well as cracks [Fig. 7(a)]. After rolling, the distinct orientations are reduced and the corrosive deformation of the surface becomes prominent. The SEM image of the 47% rolled specimen [Fig. 79(b)] shows deep pitted structures in line with the highest J_{corr} values in the corrosion test, supporting the poor corrosion resistance. Despite the cracks in the unrolled specimen [Fig. 7(a)], the low number of hollow structures on the specimen surface is consistent with the low E_{corr} and J_{corr} values.

The coating structure of the post-coated specimens is in the foreground as it was before corrosion and it is more flat than the uncoated specimens. White particles on the specimen surfaces appeared in large numbers on the coated specimens and these white spots were thought to be corrosion products deposited on the surface during the degradation process [Fig. 7(c)] [42]. No distinctive change was observed in the unrolled and rolled specimens and the coating structure remained more rigid than the specimens with uncoated surface. Despite the decrease in the E_{corr} value of the 47% rolled specimen after coating, the J_{corr} value decreased by 42.94% compared to the pre-coating state and a smoother surface was obtained in the post-coated specimens and SEM images supported this decrease. The rolled specimen, which exhibited a greater degree of deformation compared to the other coated specimens and confirmed by scanning electron microscopy (SEM) images, had the most susceptibility to corrosion, as seen by its low E_{corr} and high J_{corr} values. Considering that rolling has no effect on EDS, only the EDS of uncoated and bioceramic-coated samples were compared. The corrosion test findings prior to coating revealed the presence of biodegradation products, namely Mg, P, Ca, K, and Cl, in all samples. The post-coating spectra revealed the presence of K, Mg, and Na structures, in addition to the elements present in the coating structure. These elements were identified as biodegradation products, and the corrosion products seen were consistent with those observed in the uncoated samples.

Antimicrobial analysis

The antibacterial activity against *E. coli* was studied for ZC (Zn1Cu) alloys coated by the sol–gel method were compared to uncoated ZC as shown in Fig. 8. In Zn1Cu alloy rolled at 47% and 61%, an increase in inhibition zones was observed when the rolling ratio increased. The bacteria were incubated in a growth medium with the ZC base groups. The average of inhibition rate was 26.5 mm in ZC61% Sol–Gel, 24.5 mm in ZC47%, 22.4 mm in ZC0 (unrolled), 22 mm in ZC61% Base, 21.75 mm in ZC47% Base, 21.1 mm in ZC0 Base in the *E.coli* incubation. Looking at the inhibition rates, the highest value was found in the coated 61% rolled specimen with 26.5 mm. Table 1 (supplementary file) and SEM images (Fig. 7) obtained as a result of corrosion tests indicated that the sample with the lowest resistance was the coated 61% rolled sample and antibacterial tests also supported this result. The uncoated and unrolled specimen had the lowest inhibition ratio (21.1 mm), which also supported the corrosion and SEM results. According to the antibacterial test, inhibition rates increased with rolling reduction in both coated and uncoated samples and cell viability decreased. The fact that the
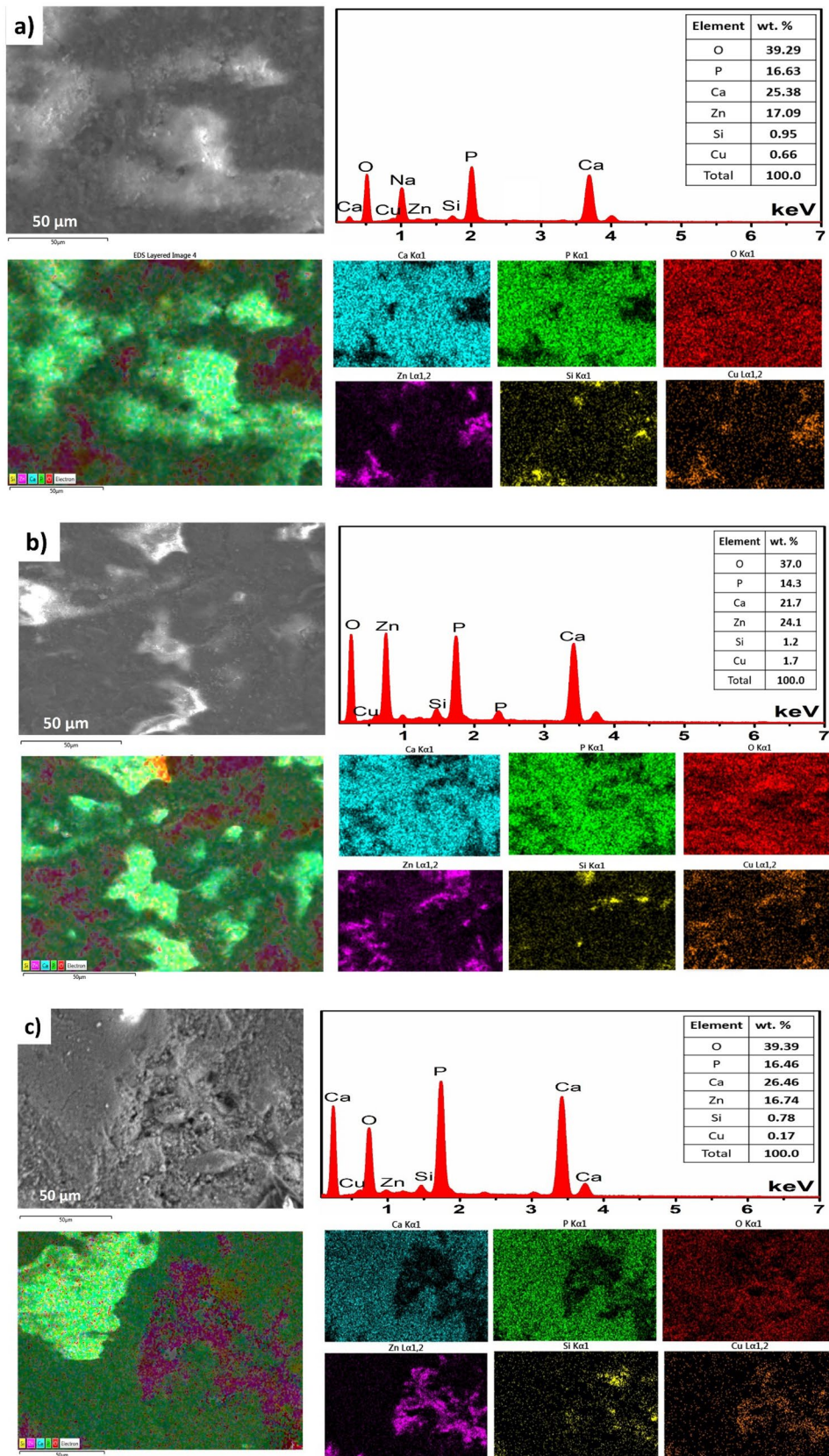
Figure 7: SEM–EDS mapping images of Zn-1Cu specimens without HA-coated rolled (a), with HA-coated 47% rolled (b), with HA-coated 61% rolled (c), after corrosion.
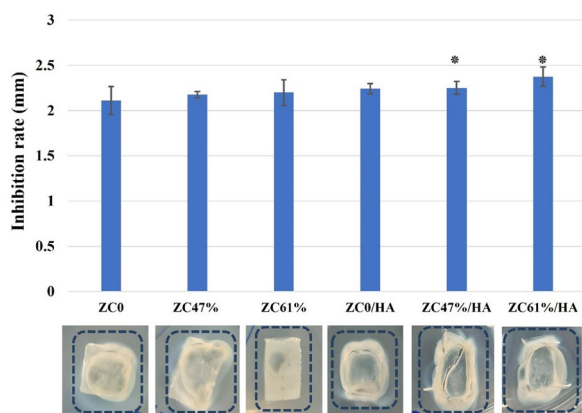
Figure 8: Histogram of inhibition rates obtained after antibiotic susceptibility test with against *E. coli* incubation, *$p < 0.05$.

coated specimens had higher inhibition rates than the uncoated specimens also showed a behavior consistent with the corrosion and SEM results obtained.

Cell viability analysis

The effect of deformation rate and coating on Zn1Cu(ZC) alloys was evaluated using L929 cell viability by MTT assay. According to ISO 10993-5:2009, a cytotoxic effect emerges when cell viability is decreased to 70% of the control group [43]. Despite a decrease in cell viability in all groups for 48 h, the samples did not induce toxicity in 48 h. However, in 72 h, the cell viability ratio decreased below 70% in some samples. The cell viability rates were found as 81.98% in ZC61 coated, 90.72% in ZC47 coated, 81.21% in ZC0 coated, 80.04% in ZC61 Base, 83% in ZC47 Base, 114.4% in ZC0 Base groups in 24 h. The cell viability rates were detected as 71.75% in ZC61, 82.13% in ZC47, 76.4% in ZC0, 72.07% in ZC61 Base, 77.82% in ZC47 Base, 104.6% in ZC0 Base groups in 48 h [Fig. 9(a, b]. Furthmore, the cell viability of 47% rolled and sol–gel coated alloys significantly increased by around 4–8% in 24 and 48 h. The cell viability was found good in all materials at 24 h as the images were shown Fig. 11 (supplementary file).

While-coated specimens showed better cell viability, coated and uncoated rolled specimens reached the highest cell viability values in line with their high-corrosion resistance. The absence of voids and cracked structures on the surface in the optical images obtained supports this result. In addition, the non-rolled specimen, which has the lowest wettability angle, supported the cell viability value with a smoother surface. The 47% rolled specimen with coating showed more corrosion resistance, which directly affected the cell-viability tests. It can be seen in Fig. 9(b) that the rolled (47%) and then coated specimen achieved higher cell viability than rolled but uncoated specimens [Fig. 9(a)]. In the SEM images after the corrosion tests, the coated 47% rolled specimen maintained its integrated structure and had good cell
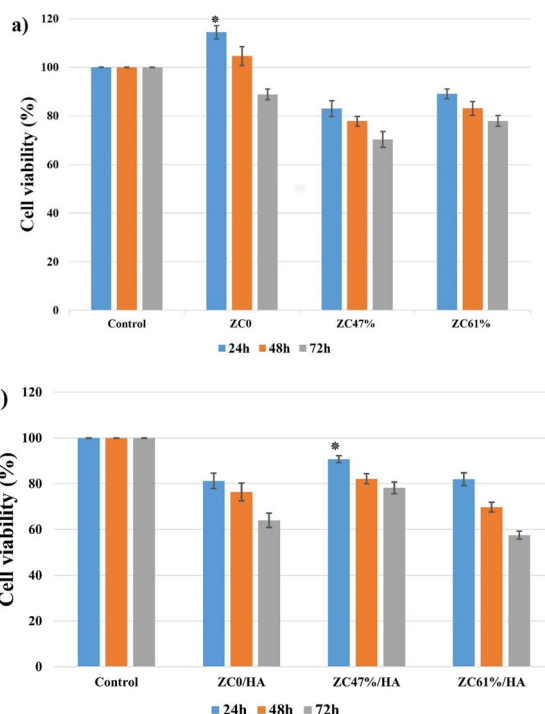

Figure 9: The effect of the Rolling and HA-coating on cell viability for (a) Base ZC0, ZC47, ZC61 and (b) Sol–Gel HA-coated and rolled for ZC0, ZC47, ZC61 in 24, 48 and 72 h. *$p < 0.05$.

viability, reflecting the positive effects of the coating. At the end of 48 h, the coated 61% rolled specimen showed the lowest value and after 72 h it was below 70% cell viability. This is due to the excess of hollow structures in the SEM images of the specimen, indicating the negative effect of high rolling on cell viability and corrosion resistance. This is also thought to prevent the coating from adhering to the sample surface [44].

Conclusions

After being produced by arc casting, Zn-1Cu samples rolled at 47% and 61% ratios were coated with HA-based bioceramics by sol-gel method. The changes in the mechanical, optical and corrosion properties of the unrolled and rolled samples were investigated; optical and corrosive behavior of these samples after HA coating were observed. It was determined that the fine-grained structure of the rolled specimens compared to unrolled-cast specimens and the secondary phase structure (CuZn5) seen in the microstructure as a result of rolling contributed positively to the mechanical properties. Before coating, SEM and EDS examinations revealed porous structures such as voids, cracks, and orientations on the surface of the samples, however these voids were seemed to be filled after coating. The 47% rolled specimen had the maximum compressive strength and hardness values, which were higher than the 61% rolled specimen. According to

the wettability analysis, the uncoated-unrolled and rolled specimens were hydrophobic, with the unrolled specimen being the least hydrophobic.

Both uncoated and coated specimens exhibited comparable corrosion resistance, with no discernible impact of coatings on corrosion resistance. The SEM views revealed that the coating surface exhibited more integrity compared to the untreated surface following the corrosion test. Through the results, it was also shown that the uncoated specimens showed better corrosion resistance than other specimens with high E_{corr}, low I_{corr} and corrosion rate. The inhibition rates of the ZC groups were higher than inhibition rates of the ZC Base groups on *E. coli*. Cell viability test showed that the HA coated groups produced higher cell viability ratios than the uncoated ZC Base groups. The cell viability of 47% rolled and sol gel coated alloys significantly increased by 4–8% in 24 and 48 h.

Although the findings indicate the advantages of Zn-based biodegradable alloys, nevertheless, there are still several challenges Particularly low mechanical properties and degradation rate control are the challenges and need to be addressed before clinical trials of Zn-based materials. Therefore, in future works; new reinforcing elements and coating techniques may be studied. Also further research on production method is worthy e.g additive manufacturing could be beneficiary instead of conventional processes. Furthermore, it would be interesting to pursue better understanding of the loss of mechanical integrity during implant degradation and this could be crucial for preventing implant's failure during service. It is also worthwhile to understand the effect of physiological elements in vitro and in vivo degradation rates.

Materials and method

Materials

High purity Zinc (Zn-Thermo Scientific 99.99%, 10×2 mm, LOT: P30H058) and copper Copper (Cu-Thermo Scientific 99.99%, LOT: Z24F031, 1–10 mm) granules were used to produce Zn1Cu alloy. Before casting, Zn and Cu were weighed on a precision balance and 5 Zn-1Cu packs of 200 g each were formed and 198 g Zn and 2 g Cu grains in one pack were separated by different packs. In the casting process, the whole atmosphere was kept for 30 min to reach the same temperature in a laboratory type oven that can reach up to 850 °C.

For homogeneous mixing of the Zn–Cu alloys, first half of the Zn grains were added to the crucible, then the rest of Cu and Zn were added and covered. The crucible was placed in the furnace and the vacuum was activated. After the Zn–Cu mixture was introduced into the furnace, melting-mixing processes were carried out in 3 stages at 30-min intervals to control and to form a homogeneous structure in the mixing processes. The crucible was taken out of the furnace, poured into a $11.2 \times 11.2 \times 107$

mm multi-mold at room temperature and removed from the mold after controlled cooling of the alloy. The produced Zn-1Cu cast samples were homogenization annealed at 350 °C for 16 s (Vulcan 3–550) and cooled with water at room temperature. The samples were cleaned with ethanol and made ready for rolling.

Cold rolling

Zn-1Cu samples with dimensions of $11.2 \times 11.2 \times 11.2 \times 107$ mm obtained by casting were rolled in a laboratory type rolling mill and deformed by reaching 41% in 4 passes and 61% in 7 passes. The sheets obtained from rolling were precision cut by wire EDM (Charmilles Technol, Robofil-510, Ikitelli, Istanbul) at a rate of 10 mm/min and prepared for coating, corrosion tests, antibacterial and cell viability analysis and other characterization analyses.

HA coating

Before coating, the beakers and equipment were cleaned with alcohol and dried, and the chemicals used in the sol–gel process were weighed with a precision balance. HA coatings were applied to cast and rolled (47% and 61%) Zn1Cu samples by sol–gel method. The Zn-1Cu biodegradable samples produced by arc casting method were ultrasonically cleaned with acetone for 30 min, soaked in HNO_3 solution for 12 s and dried in an oven at 70 °C for 6 h before sol–gel coating. Initially, 14.36 wt% HA in the beaker was dissolved by adding 15 ml of distilled water and stirred with a magnetic stirrer for 30 min until a homogeneous solution was obtained. In another beaker, 5.37 wt% P_2O_5 was dissolved in 5 ml of water and added to the solution and stirring continued for 30 min after adding P_2O_5 to the solution. Then 0.59 wt% KH_2PO_4 was added to the solution and 0.69 wt% Na_2CO_3 was added to the solution after magnetic stirring. After adding Na_2CO_3, the solution was homogenized in an ultrasonic homogenizer for 2 min. For the coating process, the samples were coated by sol gel dipping method with constant ascending and descending speed (10 mm/min). After HA coating, the samples were sintered at 350 °C for 1 s and then dried in an oven at 60 °C for 3 h. The image with an average film thickness of 23.5 μm is shown in Fig. 10.

Structural characterization

Uncoated cast and 47%, 61% cold rolled Zn1Cu alloys were sanded with 120–2500 grit sandpaper at 200 rpm. After sanding, the samples were washed with water, cleaned with alcohol and dried. In the polishing process, 50% water and 50% H_3PO_4 solution was used, and electrolytic polishing method was applied for 2.1 A 30 min for cast samples, 1.75 A 25 min for 47% rolled samples and 1.85 A 25 min for 61% rolled samples, respectively.
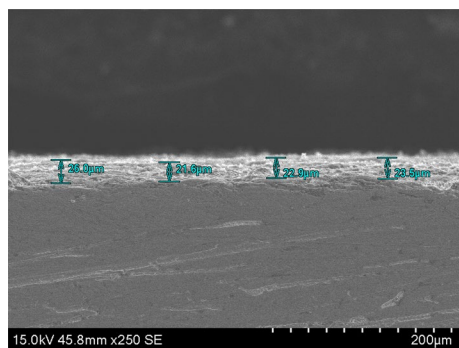
Figure 10: SEM view of HA coating layer coated on Zn1Cu.

After polishing, a solution containing 10% H_3PO_4 diluted with ethanol was prepared for etching and the samples were kept in the solution for 6 s and washed and cleaned. The microstructures of the cast and 47%, 61% rolled samples were analysed with an optical microscope (Nikon) and images were taken in the rolling direction.

Scanning electron microscopy (SEM: Hitachi-SU3500, Japan), energy dispersive spectroscopy (EDS; Oxford, UK) were used for morphological and elemental analysis of cast, cold rolled and HA coated samples of Zn1Cu alloy. Phase structures of uncoated cast and 47%, 61% cold rolled Zn1Cu alloys were measured in an X-ray diffractometer (XRD; Rigaku miniflex600, Japan) with Cu-Kα radiation. XRD patterns were recorded over a 2θ range of 20°–90° with a step size of 0.02° and a scan rate of 2° min^{-1}.

Mechanical analysis

For Vickers Hardness (EMCO-TEST DuraScan) of cast, 47% and 61% cold rolled samples of Zn1Cu alloy, 4 hardness values were taken from the surface of the samples and the hardness values of the samples were determined by averaging these values with standard deviations. The compressive strength values of Zn1Cu alloy were determined with 3 repetitions in Shimadzu-50kN device at 1 mm/min compression speed.

Corrosion tests

Simulated body fluid (SBF) was used in corrosion tests. The in vitro corrosion behavior of uncoated and HA-coated Zn-1Cu alloys was investigated using a Gamry-1010E brand and model potentiostat. Electrochemical measurements according to the potentiodynamic scanning (PDS) test procedure were performed in SBF and at body temperature (36.5 ± 0.5 °C). In the three-electrode setup, Ag/AgCl reference electrode and 25 cm^2 Pt counter electrode were used, while the produced alloys served as working electrodes. In the experimental procedure, PDS scanning was initiated at a scan rate of 0.2 mV s^{-1} from a potential

of -1.15 V against open circuit potentials (OCP) and scans were continued until the anodic potential of − 0.85 V. Corrosion potential, corrosion current and corrosion rate values were calculated from TAFEL fits of the obtained PDS curves.

Wettabality tests

Wettability analyses were performed on the Complete Range of Optical Tensiometers from Biolin Scientific, model Attension Theta Flex. The measurement accuracy of this device is ± 0.1° and the surface tension measurement accuracy is ± 0.01 mN/m. A 5 μm water drop was placed on the sample surface and the surface was recorded for 10 s. 14 frames were recorded with a camera with a maximum measurement speed of 3009 fps.

Antibacterial activity

The disc diffusion test was used to evaluate the antibacterial activity of the alloys [45]. *E. coli* (ATCC 25922) suspensions were adjusted to 0.5 McFarland standard density from 18-h nutritional broth cultures to achieve a suitable bacterial density $(1.5 \times 10^8$ CFU·ml^{-1}). Mueller–Hinton agar plates were inoculated with 0.1 ml of the bacterial suspensions. After being rinsed in an ultrasonic bath with water and ethyl alcohol for 3 min, the samples were sterilized for 30 min under UV radiation with a wavelength of 254 nm. The test samples were prepared and then put on petri dishes with bacterium plates. After 24 h of incubation at 37 °C, the inhibition zone surrounding the discs was measured using a digital micrometer [46]. To choose the best samples several groups have been formed, and tests were carried out three times.

Cell viability analysis

According to the UNI EN ISO 10993 regulation [43], the cytotoxicity experiment was performed using the L929 mouse fibroblast cell line. L929 cell lines were maintained in DMEM/F12 media supplemented with 10% fetal bovine serum and 1% penicillin/streptomycin at 37 °C and 5% CO_2. Trypsinization was carried out to remove confluent cells from the surface, and a hemocytometer was used to count the number of cells in the pellet after centrifuging the cells. The cells were then subsequently subjected to cytotoxicity tests.

L929 cells were placed in 96-well plates with 10,000 cells per well in which the prepared samples were kept in the cell culture medium. Plates were then incubated at 37 °C for 24, 48 and 72 h. The MTT (3-(4,5-dimethylthiazol-2-yl)-2,5-diphenyltetrazolium bromide) technique was used to determine the cytotoxic [47]. The cell culture medium was replaced with

100 µl fresh medium and 15 µl of MTT solutions and incubated for 2 h in the dark. After incubation, the absorbance values of the wells were calculated using a micro-plate reader and a reading at 570 nm. Each assay was repeated five times. A sample is defined as cytotoxic if the percentage vitality value is 70% or below, and noncytotoxic if the percentage vitality value is greater than 70% [48]. After 24 h incubation, the materials applied L929 fibroblast cell images were observed in inverted microscope (Leica DMI6000).

Statistical analysis

The samples were analyzed with one-way ANOVA test and independent-sample t-test were used to describe significant differences between samples. Results were presented as mean ± standard deviation. The level of significance was selected as $p < 0.05$.

Author contributions

B. A: Project administration, Methodology, Writing—original draft, Validation. S.A.K: Experimental work, graphical presentation of the results. N. A: Charecterization analysis, Writing & editing. F. F: Charecterization analysis and Corrosion tests. S.S: Deformation – rolling process. Y.Y: In vitro cytotoxicity analysis.

Funding

Data availabilty

The authors confirm that the data supporting the findings of this study are available within the article [and/or its supplementary materials]. However, for additional data queries that support the findings of this study can be provided from the corresponding author, [B. Aksakal], upon reasonable request.

Code availability

Not applicable.

Declarations

Competing interest The authors declare that they have no potential competing interests that could interfere with his/her full capacity of being perfectly objective regarding his/her research and manuscript. declares potential conflicts of interest that could interfere with his/her full capacity of being perfectly objective regarding his/her research and manuscript.

Ethical approval

The work is original and has not been published previously or is not under consideration for publication elsewhere. If accepted, it will not be published elsewhere in any form without a copyright holder.

Consent to participate

All authors have read and agreed to the submitted version of the manuscript. Informed consent was obtained from all individual participants included in the study.

Consent for publication

Not applicable in this manuscript.

Supplementary Information

The online version contains supplementary material available at https://doi.org/10.1557/s43578-024-01340-6.

References

1. L. Ghasemi-Mobarakeh, D. Kolahreez, S. Ramakrishna, D. Williams, Key terminology in biomaterials and biocompatibility. Curr. Opin. Biomed. Eng. **10**, 45–50 (2019). https://doi.org/10.1016/J.COBME.2019.02.004

2. E. Marin, F. Boschetto, G. Pezzotti, Biomaterials and biocompatibility: an historical overview. J. Biomed. Mater. Res. A **108**(8), 1617–1633 (2020). https://doi.org/10.1002/JBM.A.36930

3. N. Aslan, B. Aksakal, M.E. Aksoy, Boron-incorporated biocomposite coatings on 316L and NiTi alloys: Enhanced structural, antibacterial activity, and cell viability performances. Proc Inst. Mech. Eng. Part H **236**(10), 1572–1580 (2022). https://doi.org/10.1177/09544119221122061

4. Y.X. Yin et al., "Hemocompatibility of biodegradable Zn-0.8 wt% (Cu, Mn, Li) alloys. Mater. Sci. Eng. C. Mater. Biol. Appl. (2019). https://doi.org/10.1016/J.MSEC.2019.109896

5. H. Yang et al., Evolution of the degradation mechanism of pure zinc stent in the one-year study of rabbit abdominal aorta model. Biomaterials **145**, 92–105 (2017). https://doi.org/10.1016/J.BIOMATERIALS.2017.08.022

6. H.F. Li, Z.Z. Shi, L.N. Wang, Opportunities and challenges of biodegradable Zn-based alloys. J. Mater. Sci. Technol. **46**, 136–138 (2020). https://doi.org/10.1016/J.JMST.2019.12.014

7. M. Bahraminasab, B.B. Sahari, K.L. Edwards, F. Farahmand, M. Arumugam, Aseptic loosening of femoral components—materials engineering and design considerations. Mater. Des. **44**, 155–163 (2013). https://doi.org/10.1016/J.MATDES.2012.07.066

8. C. Godavitarne, A. Robertson, J. Peters, B. Rogers, Biodegradable materials. Orthop. Trauma **31**(5), 316–320 (2017). https://doi.org/10.1016/J.MPORTH.2017.07.011

9. M. Moravej, D. Mantovani, Biodegradable metals for cardiovascular stent application: interests and new opportunities. Int. J. Mol. Sci. **12**(7), 4250–4270 (2011). https://doi.org/10.3390/IJMS12074250

10. Y. Yun et al., Revolutionizing biodegradable metals. Mater. Today **12**(10), 22–32 (2009). https://doi.org/10.1016/S1369-7021(09)70273-1

11. P.R. Kowey, Novel therapeutic targets for antiarrhythmic drugs. Circulation **123**(7), 8 (2011). https://doi.org/10.1161/CIRCULATIONAHA.110.980037

12. P.K. Bowen et al., Biodegradable metals for cardiovascular stents: from clinical concerns to recent Zn-alloys. Adv. Healthc. Mater. **5**(10), 1121–1140 (2016). https://doi.org/10.1002/ADHM.201501019

13. E. Aghion, G. Levy, S. Ovadia, In vivo behavior of biodegradable Mg-Nd-Y-Zr-Ca alloy. J. Mater. Sci. Mater. Med. **23**(3), 805–812 (2012). https://doi.org/10.1007/S10856-011-4536-8

14. T. Savaşkan, G. Pürçek, S. Murphy, Sliding wear of cast zinc-based alloy bearings under static and dynamic loading conditions. Wear **252**(9–10), 693–703 (2002). https://doi.org/10.1016/S0043-1648(01)00876-6

15. Y. Torres, J.J. Pavón, J.A. Rodríguez, Processing and characterization of porous titanium for implants by using NaCl as space holder. J. Mater. Process. Technol. **212**(5), 1061–1069 (2012). https://doi.org/10.1016/J.JMATPROTEC.2011.12.015

16. E. Mostaed, M. Sikora-Jasinska, J.W. Drelich, M. Vedani, Zinc-based alloys for degradable vascular stent applications. Acta Biomater. **71**, 1–23 (2018). https://doi.org/10.1016/J.ACTBIO.2018.03.005

17. R. Yue et al., Microstructure, mechanical properties and in vitro degradation behavior of novel Zn-Cu-Fe alloys. Mater Charact **134**, 114–122 (2017). https://doi.org/10.1016/J.MATCHAR.2017.10.015

18. E. Mostaed, M.S. Ardakani, M. Sikora-Jasinska, J.W. Drelich, Precipitation induced room temperature superplasticity in Zn-Cu alloys. Mater. Lett. **244**, 203–206 (2019). https://doi.org/10.1016/J.MATLET.2019.02.084

19. A. Kafri, S. Ovadia, G. Yosafovich-Doitch, E. Aghion, The effects of 4%fe on the performance of pure zinc as biodegradable implant material. Ann. Biomed. Eng. **47**(6), 89 (2019). https://doi.org/10.1007/S10439-019-02245-W

20. B. Jia et al., In vitro and in vivo studies of Zn-Mn biodegradable metals designed for orthopedic applications. Acta Biomater. **108**, 358–372 (2020). https://doi.org/10.1016/J.ACTBIO.2020.03.009

21. H. Kabir, K. Munir, C. Wen, Y. Li, Recent research and progress of biodegradable zinc alloys and composites for biomedical applications: Biomechanical and biocorrosion perspectives.

22. A. Kumar, S. Kargozar, F. Baino, S.S. Han, Additive manufacturing methods for producing hydroxyapatite and hydroxyapatite-based composite scaffolds: a review. Front. Mater. **6**, 313 (2019)

23. D. Arcos, M. Vallet-Regí, Substituted hydroxyapatite coatings of bone implants. J. Mater. Chem. B **8**(9), 1781–1800 (2020)

24. P. Li et al., Investigation of zinc-copper alloys as potential materials for craniomaxillofacial osteosynthesis implants. Mater. Sci. Eng. C **103**, 109826 (2019). https://doi.org/10.1016/J.MSEC.2019.109826

25. D. Palai et al., Influence of copper on the microstructural, mechanical, and biological properties of commercially pure Zn-based alloys for a potential biodegradable implant. ACS Biomater. Sci. Eng. **8**(4), 1443–1463 (2022). https://doi.org/10.1021/ACSBIOMATERIALS.1C01111

26. C. Shuai, Y. Cheng, Y. Yang, S. Peng, W. Yang, F. Qi, Laser additive manufacturing of Zn-2Al part for bone repair: formability, microstructure and properties. J. Alloys Compd. **798**, 606–615 (2019). https://doi.org/10.1016/J.JALLCOM.2019.05.278

27. C. Shuai et al., A peritectic phase refines the microstructure and enhances Zn implants. J. Mater. Res. Technol. **9**(3), 2623–2634 (2020). https://doi.org/10.1016/J.JMRT.2020.04.037

28. J. Niu et al., Research on a Zn-Cu alloy as a biodegradable material for potential vascular stents application. Mater. Sci. Eng. C **69**, 407–413 (2016). https://doi.org/10.1016/J.MSEC.2016.06.082

29. L. Chen, X. Ma, Z. Ma, D. Lu, B. Hou, Study on microstructure and corrosion resistance of high-hardness Zn-1.0Cu-1.0Ti alloy. Mater Charact **178**, 111283 (2021). https://doi.org/10.1016/J.MATCHAR.2021.111283

30. A. Kazemi-Navaee, R. Jamaati, H.J. Aval, Asymmetric cold rolling of AA7075 alloy: the evolution of microstructure, crystallographic texture, and mechanical properties. Mater. Sci. Eng. A **824**, 8 (2021). https://doi.org/10.1016/J.MSEA.2021.141801

31. J. Jiang, H. Huang, J. Niu, Z. Jin, M. Dargusch, G. Yuan, Characterization of nano precipitate phase in an as-extruded Zn-Cu alloy. Scr. Mater. **200**, 113907 (2021). https://doi.org/10.1016/J.SCRIPTAMAT.2021.113907

32. J. Cheng, B. Liu, Y.H. Wu, Y.F. Zheng, Comparative in vitro study on pure metals (Fe, Mn, Mg, Zn and W) as biodegradable metals. J. Mater. Sci. Technol. **29**(7), 619–627 (2013). https://doi.org/10.1016/J.JMST.2013.03.019

33. D.K. Pathak, P.M. Pandey, Evaluation of in vitro corrosion behavior of zinc–hydroxyapatite and zinc–hydroxyapatite–iron as biodegradable composites. J. Biomed. Mater. Res. Part **109**(3), 436–450 (2021). https://doi.org/10.1002/JBM.B.34712

34. J. Lin et al., A biodegradable Zn-1Cu-0.1Ti alloy with antibacterial properties for orthopedic applications. Acta Biomater. **106**, 410–427 (2020). https://doi.org/10.1016/J.ACTBIO.2020.02.017

Bioact. Mater. **6**(3), 836–879 (2021). https://doi.org/10.1016/J.BIOACTMAT.2020.09.013

35. M. Fan et al., Biocompatibility of zinc matrix biodegradable composites reinforced by graphene nanosheets. Mater. **15**, 6481 (2022). https://doi.org/10.3390/MA15186481

36. S. Liu, S.B. Xue, P. Xue, D.X. Luo, Present status of Sn–Zn lead-free solders bearing alloying elements. J. Mater. Sci. Mater. Electron. **26**(7), 4389–4411 (2015). https://doi.org/10.1007/S10854-014-2659-7

37. S. Amirkhanlou, M.R. Rezaei, B. Niroumand, M.R. Toroghinejad, High-strength and highly-uniform composites produced by compocasting and cold rolling processes. Mater. Des. **32**(4), 2085–2090 (2011). https://doi.org/10.1016/J.MATDES.2010.11.046

38. B.J. Basu, V. Hariprakash, S.T. Aruna, R.V. Lakshmi, J. Manasa, B.S. Shruthi, Effect of microstructure and surface roughness on the wettability of superhydrophobic Sol-gel nanocomposite coatings. J. Sol-Gel Sci. Technol. **56**(3), 278–286 (2010). https://doi.org/10.1007/S10971-010-2304-8/METRICS

39. S. Cihangir, Greening industrially applied toxic cadmium plating with γ-Ni2Zn11 alloy in deep eutectic solvents: promising electroplating efficiency and chemical corrosion resistance. Adv. Eng. Mater. **25**(20), 2300731 (2023). https://doi.org/10.1002/ADEM.202300731

40. S. Cihangir, Y. Say, İ Ozkul, O. Guler, S.H. Guler, Microstructure and corrosion investigation of FeCoCrNiMo0,5(MnAl)0,3 high entropy alloy produced by 316 L stainless steel scrap. Mater. Today Commun. **33**, 104360 (2022). https://doi.org/10.1016/J.MTCOMM.2022.104360

41. Y. Say, B. Aksakal, Effects of hydroxyapatite/Zr and bioglass/Zr coatings on morphology and corrosion behaviour of Rex-734 alloy. J. Mater. Sci. Mater. Med. **27**(6), 89 (2016). https://doi.org/10.1007/S10856-016-5716-3

42. Z. Tang et al., Potential biodegradable Zn-Cu binary alloys developed for cardiovascular implant applications. J. Mech. Behav. Biomed. Mater. **72**, 182–191 (2017). https://doi.org/10.1016/J.JMBBM.2017.05.013

43. "ISO 10993-5:2009-Biological evaluation of medical devices—Part 5: Tests for in vitro cytotoxicity." Accessed: Nov. 14, 2023. Available: https://www.iso.org/standard/36406.html

44. Y. Shi et al., Surface modification on biodegradable zinc alloys. J. Mater. Res. Technol. **25**, 3670–3687 (2023). https://doi.org/10.1016/J.JMRT.2023.06.149

45. R. Humphries, A.M. Bobenchik, J.A. Hindler, A.N. Schuetz, Overview of changes to the clinical and laboratory standards institute performance standards for antimicrobial susceptibility testing, M100, 31st edition. J. Clin. Microbiol. **59**(12), 11 (2021). https://doi.org/10.1128/JCM.00213-21

46. M. Balouiri, M. Sadiki, S.K. Ibnsouda, Methods for in vitro evaluating antimicrobial activity: a review. J. Pharm. Anal. **6**(2), 71–79 (2016). https://doi.org/10.1016/J.JPHA.2015.11.005

47. E. Kilicay, E. Erdal, B. Hazer, M. Türk, E.B. Denkbas, Antisense oligonucleotide delivery to cancer cell lines for the treatment of different cancer types. Artif. Cells Nanomed. Biotechnol. **44**(8), 1938–1948 (2016). https://doi.org/10.3109/21691401.2015.1115409

48. V. Cannella et al., In vitro biocompatibility evaluation of nine dermal fillers on L929 cell line. Biomed. Res. Int. (2020). https://doi.org/10.1155/2020/8676343